Key Points:
- Elevated geothermal heat flux
- Spatial variation of geothermal heat flux on small scales

Correspondence to:
R. Dziadek,
ricarda.dziadek@awi.de

Geothermal heat flux in the Amundsen Sea sector of West Antarctica: New insights from temperature measurements, depth to the bottom of the magnetic source estimation, and thermal modeling

R. Dziadek[1] (iD), K. Gohl[1] (iD), A. Diehl[2], and N. Kaul[2] (iD)

[1]Alfred Wegener Institute - Helmholtz Centre for Polar and Marine Research, Am Alten Hafen, Bremerhaven, Germany, [2]University of Bremen, Department of Geosciences, Bremen, Germany

Abstract Focused research on the Pine Island and Thwaites glaciers, which drain the West Antarctic Ice Shelf (WAIS) into the Amundsen Sea Embayment (ASE), revealed strong signs of instability in recent decades that result from variety of reasons, such as inflow of warmer ocean currents and reverse bedrock topography, and has been established as the Marine Ice Sheet Instability hypothesis. Geothermal heat flux (GHF) is a poorly constrained parameter in Antarctica and suspected to affect basal conditions of ice sheets, i.e., basal melting and subglacial hydrology. Thermomechanical models demonstrate the influential boundary condition of geothermal heat flux for (paleo) ice sheet stability. Due to a complex tectonic and magmatic history of West Antarctica, the region is suspected to exhibit strong heterogeneous geothermal heat flux variations. We present an approach to investigate ranges of realistic heat fluxes in the ASE by different methods, discuss direct observations, and 3-D numerical models that incorporate boundary conditions derived from various geophysical studies, including our new Depth to the Bottom of the Magnetic Source (DBMS) estimates. Our in situ temperature measurements at 26 sites in the ASE more than triples the number of direct GHF observations in West Antarctica. We demonstrate by our numerical 3-D models that GHF spatially varies from 68 up to 110 mW m^{-2}.

1. Introduction

The Amundsen Sea Embayment is part of the West Antarctic Rift System (WARS, Figure 1), the second largest continental rift system on earth [*LeMasurier*, 2008], which displays unique coupled relationships between tectonic processes and ice sheet dynamics. Palaeo-ice streams have eroded troughs across the ASE that today route warm ocean deep water to the WAIS grounding zone and reinforce dynamic ice sheet thinning [*Bingham et al.*, 2012]. Rift basins, which cut across West Antarctica's landward sloping shelves, promote ice sheet instability [*Bingham et al.*, 2012]. The overall timing and magnitude of the plate motions leading to the development of the rift system remains poorly known [*Cande et al.*, 2000]. The WARS formed as a plate boundary that separates East and West Antarctica and underwent at least two major extension phases (~100–80 Ma, ~40–30 Ma), that followed a long-lived paleo-Pacific subduction system along margin of the Gondwana supercontinent [*Mukasa and Dalziel*, 2000]. The subduction of spreading ridges, e.g., the Pacific-Phoenix spreading ridge, is hypothesized to have caused the shutting off subduction-related magmatism at 110 ± 1 Ma along Ruppert and Hobbs Coast, but continued until 96 ± 1 Ma in the Pine Island Bay area to the east of Marie Byrd Land. *Jordan et al.* [2010] proposed that wide mode distributed rifting, mostly occurring during mid to late Cretaceous stages, resulted in crustal thinning onshore (~25 km). Particularly, the following Cenozoic narrow-mode rifting caused further thinning of the crust to less than 20 km beneath Pine Island Glacier, which superimposes the Pine Island Rift. Narrow-mode rifting may have occurred in the Cenozoic, synchronous with oceanic spreading in the Adare Trough located in the Ross Sea Sector of the WARS between 48 and 24 Ma [*Cande et al.*, 2000; *Luyendyk et al.*, 2003; *Davey et al.*, 2016]. The possible rifts extensions to the Bellingshausen Sea Embayment [*Bingham et al.*, 2012] might be kinematically linked with the progressive shut down of the Cenozoic subduction along the western margin of the Antarctic Peninsula [*Ferraccioli et al.*, 2006; *Eagles et al.*, 2009; *Jordan et al.*, 2010]. Narrow Cenozoic rifts such as the Pine Island Rift however have not been clearly identified beneath the continental shelf of the Amundsen Sea
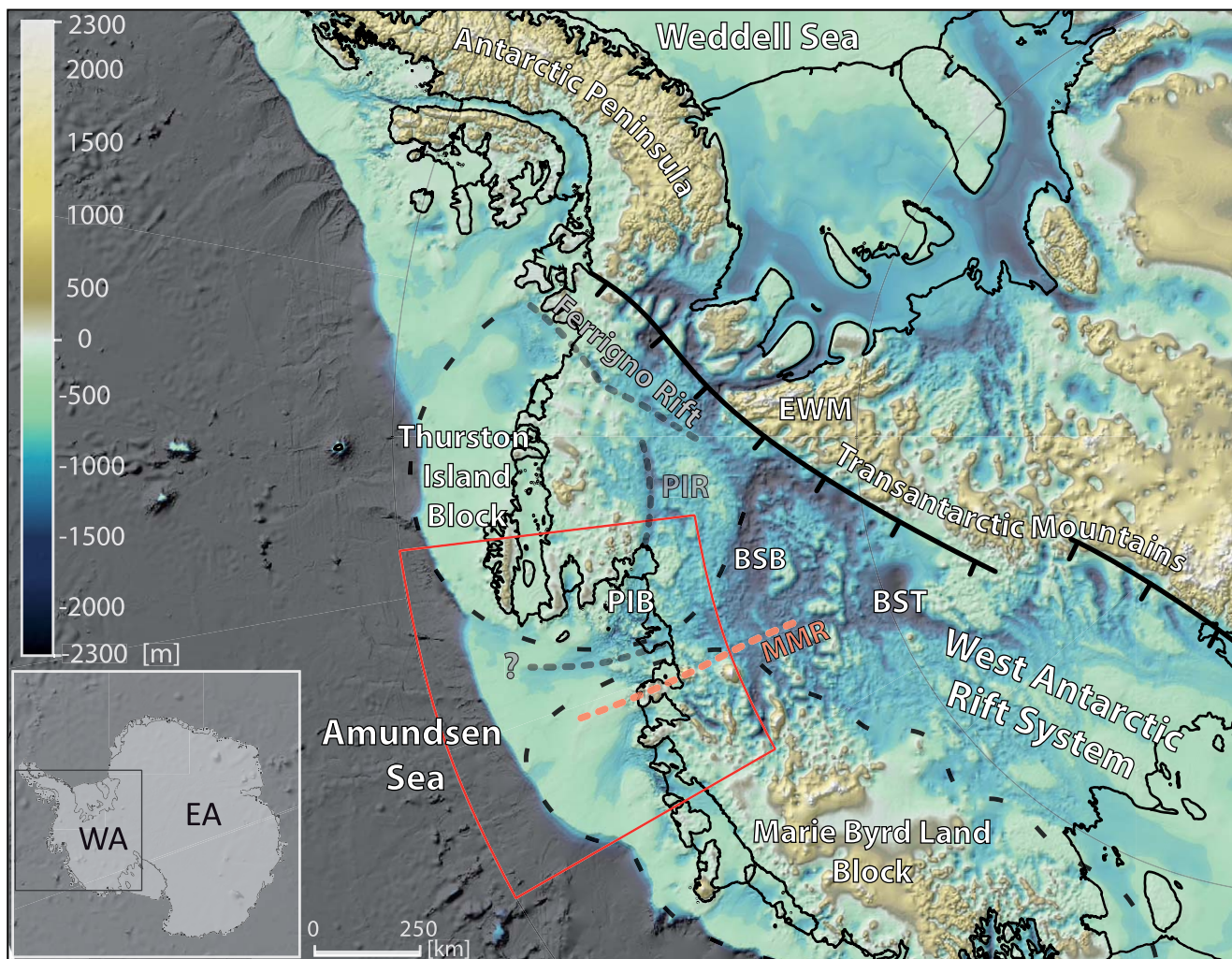
Figure 1. Location of the study area in West Antarctica highlighted by red square, which comprises the Amundsen Sea Embayment, adjacent to Thurston Island crustal block, Pine Island Rift (PIR), Ferrigno Rift, Byrd Subglacial Basin (BSB), Bentley Subglacial Trench (BST), and Marie Byrd Land crustal block. The south-eastern boundary of the West Antarctic Rift System (black line) passes along the margins of the Ellsworth-Whitmore Mountains (EWM) [*Jordan et al.*, 2017] and the Transantarctic Mountain Range, which separates East Antarctica (EA) from West Antarctica (WA). MMR is the recently postulated Mount Murphey Rift [*Spiegel et al.*, 2016]. The supposed extension of a rift branch into the ASE is has not been confirmed yet [*Gohl*, 2012; *Gohl et al.*, 2013b]. The subglacial topography is from BEDMAP2 [*Fretwell et al.*, 2013] and bathymetry is from IBCSO [*Arndt et al.*, 2013].

Embayment in this study region. *Gohl et al.* [2013a] however investigated magnetic anomaly patterns, structural lineaments, and characterization magnetic source bodies, with respect to sedimentation and regional plate tectonic settings. They associate anomaly trends and tectonic features with at least three tectonic phases: (1) magmatic emplacement zones of Cretaceous rifting and breakup (100–85 Ma), to (2) a southern distributed plate boundary zone of the Bellingshausen Plate (80–61 Ma) and (3) activities of the WARS indicated by NNE-SSW trending lineaments (55–30 Ma). By Oligocene time uplift, associated with the initiation of the present volcanic activity, in Marie Byrd Land was about to commence [*Mukasa and Dalziel*, 2000]. *Spiegel et al.* [2016] recently proposed that the exhumation of the Mt. Murphy area could be a response to Oligocene rifting along Pine Island Bay, probably contemporaneous with the Ferrigno Rift. According to their hypothesis, this lead to northeastward movement of the Thurston Island block, and extension beneath the main trunk of Pine Island Glacier and in the Byrd Subglacial Basin.

Young, continental rift systems are regions with significantly elevated geothermal heat flux [*Morgan*, 1983] because the transient thermal perturbation to the lithosphere caused by rifting requires ∼100 Ma to reach long term thermal equilibrium [*McKenzie*, 1978; *Jarvis and McKenzie*, 1980; *Cochran*, 1983; *Jaupart and Mareschal*, 2007]. It is suspected to be heterogeneous as a reflection of slow decay of thermal anomaly

when stretching of the crust ceases and the distribution volcanic activity along the complex branching geometry of the WARS, which reflects its multi-stage history and structural inheritance [*Kalberg et al.*, 2015]. Geothermal heat flux strongly influences ice flow rates, basal friction, deformation rates, and/or hydrological systems, which in turn control ice-bed coupling, and therefore the height and dynamics of ice sheets [*Hughes*, 2009]. Antarctic ice sheet modeling studies usually assume values of 40–70 mW m^{-2} over large areas based on block distribution [*Hansen and Greve*, 1996; *Pollard et al.*, 2005]. However, West Antarctic GHF is suspected to be both higher ($>$100 mW m^{-2}) and more variable on small scales [*Bingham et al.*, 2012; *Fisher et al.*, 2015], and this could have a large effect on patterns of basalt melt rates and ice flow. This could explain why the WAIS is particularly susceptible to partial collapses [*Payne et al.*, 2004; *Wingham et al.*, 2009; *Hughes*, 2011], a suggestion that could be tested by the use of realistic nonuniform GHF values in ice sheet modeling and that, in turn, would considerably improve predictions of ice sheet collapse. The problem with testing these possibilities is that direct observations of GHF in Antarctica are so sparse that it counts as the greatest source of uncertainty in ice sheet studies for the continent [*Larour et al.*, 2012]. The grounded ice has retreated since the Last Glacial Maximum ($\sim$20 ka) toward its present-day location [*Lowe and Anderson*, 2002]. The investigated offshore area might be hypothetically related to those areas onshore, where the present WAIS rests on bed with similar geothermal properties. Therefore, high-resolution GHF will aid the understanding of the paleo-retreat of the ice sheet in this sector. To address the uncertainties, our objective is to discuss ranges of realistic heat flux values in the ASE based on direct observations, depth to the bottom of the magnetic source estimates and numerical 3-D models.

2. Data and Methods

2.1. In Situ Geothermal Gradient Measurements

In situ temperature measurements for deriving geothermal heat flux (GHF) were conducted during RV Polarstern expedition ANT-XXVI/3 at 26 stations [*Gohl and Participants*, 2010]. We used five Miniaturized Temperature Logger (MTL) with 0.001 K resolution and 0.1 K precision [*Pfender and Villinger*, 2002], equidistantly mounted on a 4 m long temperature sensor rod and a sampling interval of 1 s. Prior to deployment, the MTL were calibrated for absolute temperatures with the ships SBE911plus CTD (conductivity, temperature, and depth) in the water column. After calibration, the offset between MTL and CTD was $\pm$0.001 K, which is within the overall resolution of the MTL. Additional weights were mounted on the upper part of the rod to support the penetration into the sediment. A sixth MTL was mounted above the probes weight and measured the temperature of the water column (see Figure 2a). Exemplarily shown in Figure 2b are the temperatures collected by the MTL during the deployment and penetration phase of station 4. In the first stage, the probe is lowered through the water column, when entering the sediment the temperatures rise at first due to the frictional heat. Furthermore, the frictional heat was an indicator that the sensor has entered the sediment. This could be also supported by a brief visual inspection of sediment coverage of the probe once it was hoisted back on deck. We used an up to 10 min steady-time, where the probe rests in the sediment, which allows for the frictional heat to decay and the temperatures to adjust to ambient sediment temperatures. Stage 3 is marked in red colors and highlights the stabilization of the sediment temperatures. Please note that the data of the water sensor is not shown in Figure 2b. The mean temperature of the stabilization phase is plotted against the depth of the sensors (see Figure 2c). Because we do not have absolute depth information, we shift the upper sediment sensor toward 0 m depth and calculate the thermal gradient with a linear fit. In case of station 4, sensor 1 was not used for the linear regression to obtain the temperature gradient. The data collected at the 26 sites are shown in Figure 3 according to the temperatures-depth profile described in Figure 2c. The upper, filled triangles indicate the temperatures of the water sensor at the time of sediment temperature stabilization. At site 13, 14, 15, 18, and 24 it does not appear in the temperature-depth profiles, because no data could be retrieved from the sensor logger. At site 18, 19, and 26 several sediment logger were either lost or damaged during deployment, at site 18 in particular the probe also did not entirely penetrate the sediment. This should be kept in mind, when interpreting or working with the data. The thermal conductivity (k) was measured on gravity cores on board at stable ambient temperatures, taken in the vicinity of or at the 26 sites shown in Figure 4 with a KD2 Pro Thermal Property Analyzer that has an accuracy of $\pm$5% from 0.2 to 2 W m^{-1} K^{-1} [*Decagon Devices Inc.*, 2012]. The 6 cm long sensor applies a very small amount of heat to the needle which helps to prevent free convection in liquid samples. Because of the sensors heat pulse, a minimum of 1.5 cm of material parallel to the sensor in all
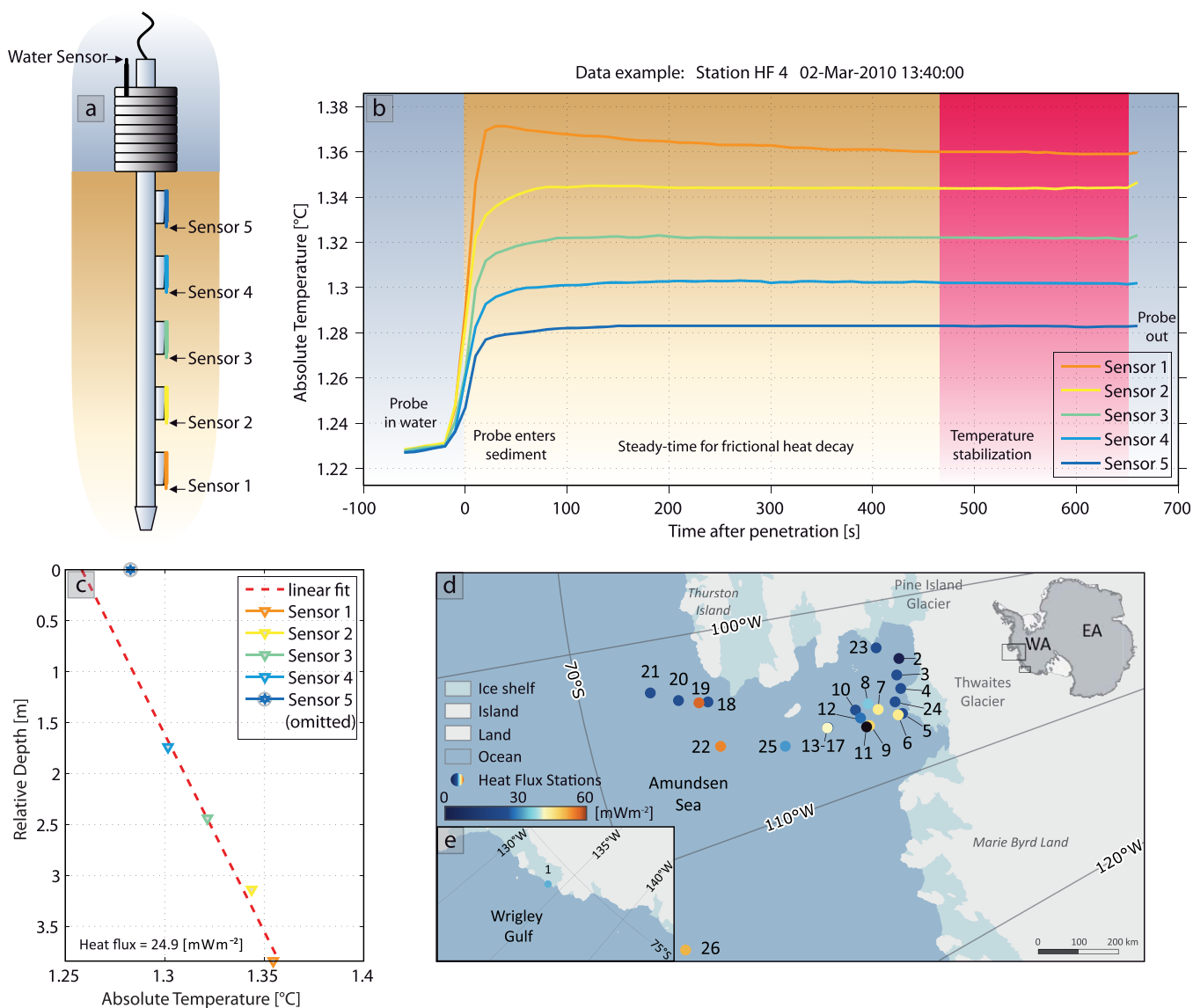
Figure 2. (a) Schematic drawing of the probe and sensor geometry. The sediment sensors are equidistantly mounted along the metal rod. The weight at the upper end enforces sediment penetration. A water sensor is mounted above the weight. Please note for simplification of this figure they appear to be in line, whereas they were mounted around the rod to minimize the disturbance of the sediment. (b) The different deployment stages are highlighted for a data example at site 4. The probe is lowered through the water column, frictional heat is created when the instrument enters the sediment. The steady-time allows for frictional heat decay. During the stabilization phase, temperature signal variations become relatively small and only occur near the sensor resolution range (± 0.001 K). (c) In situ temperatures of the individual sensors with depth in the sediment. The temperature gradient is obtained by a linear fit through the data points. In this case the upper data point was not used for the fit. (d) Overview map that shows the sites of sediment temperature measurements in close proximity to Wrigley Gulf (1, small inlet) and the Amundsen Sea Embayment (2–26) color-coded with estimated heat flux ranges.

directions was allowed to minimize errors. The sampling frequency along the cores ranged between 10 and 20 cm. We also noticed that penetration into sediments, where elevated thermal conductivity was observed in the cores, was not possible or very low with our temperature gradient probe. The heat flux was calculated from the product of thermal conductivity ($0.9 < k > 1.1$) and temperature gradient (Table 1).

2.2. Depth to the Bottom of the Magnetic Source (DBMS)

The DBMS is a proxy for geothermal heat flux, because both depend on the thickness of the magnetized crust [*Fox Maule et al.*, 2005]. As a result of increasing temperature with depth above the Curie temperature rocks lose their ferromagnetic magnetization. In general, a Curie temperature of 580°C for the most common magnetic mineral magnetite is considered applicable to continental crust [*Langel and Hinze*, 1998; *Bansal et al.*, 2011], which we also assume for this study. *Spector and Grant* [1970] introduced a prism-based calculation technique to analyze the power spectral density of magnetic data, particularly, to provide a
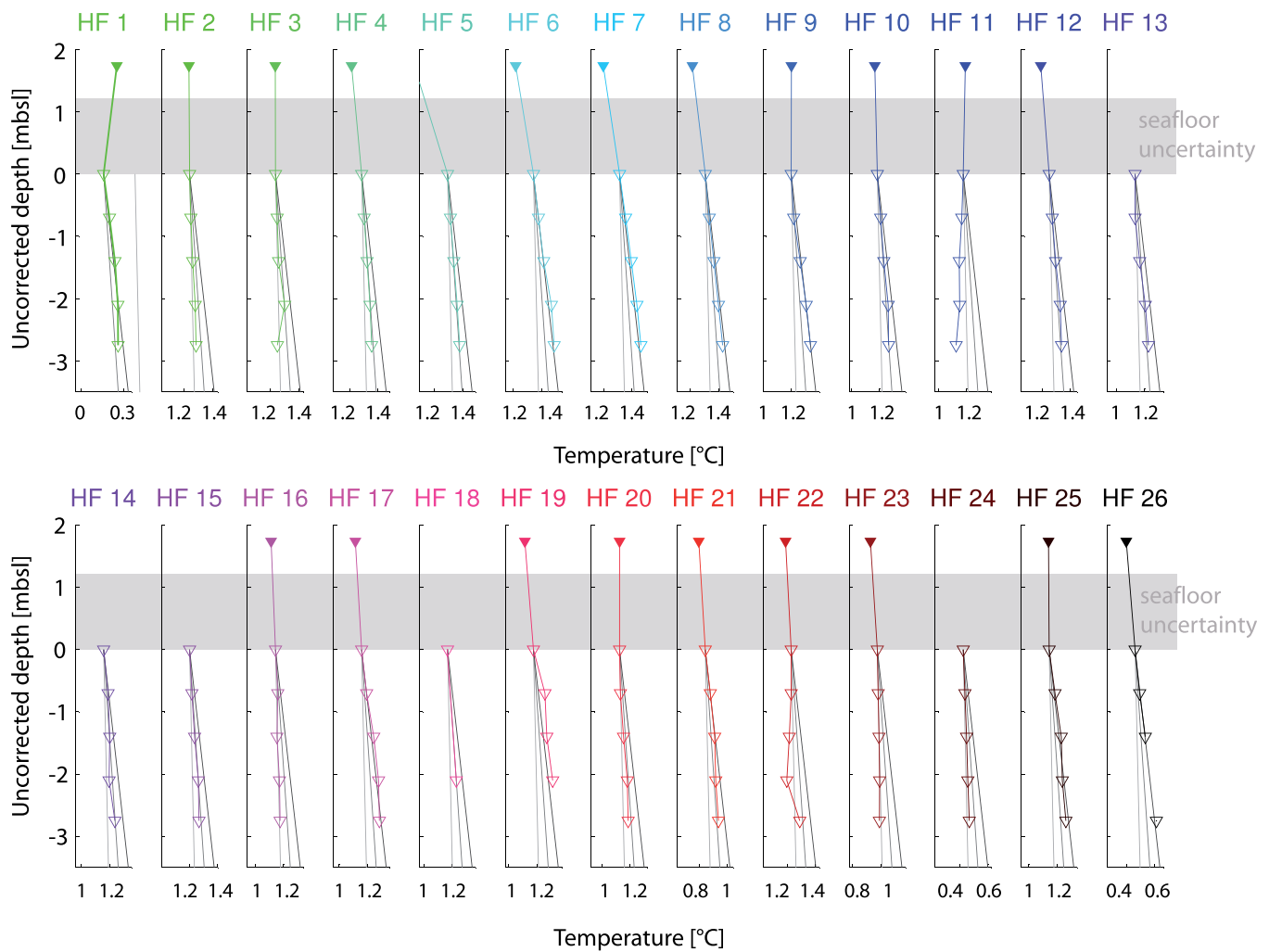
Figure 3. In situ temperature gradients measured in Wrigley Gulf (1) and Amundsen Sea Embayment (2–26). Grey lines represent a 10°C km^{-1} gradient (light grey), 30°C km^{-1} (grey) and 50°C km^{-1} (dark grey). Solid triangles above 0 mbsl represent bottom water temperatures. The uncertainty in absolute sea floor depths depend on the distance between individual MTLs mounted on the sensor rod.
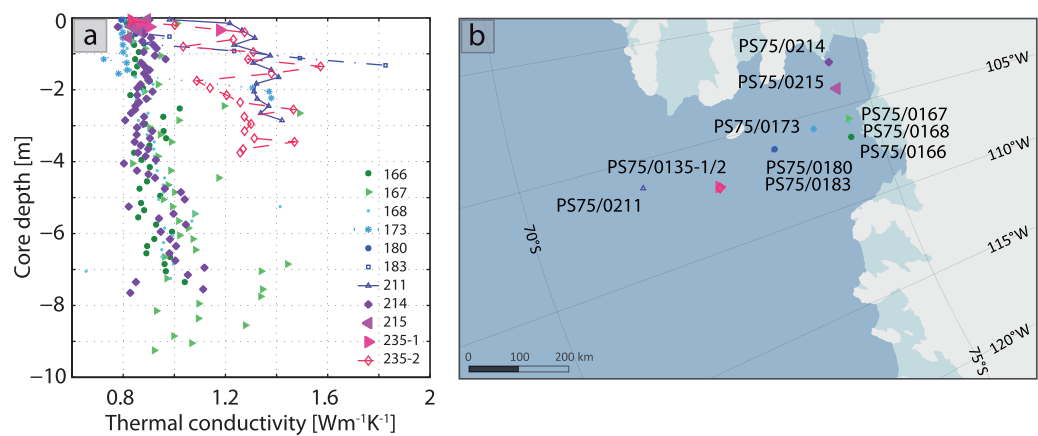
Figure 4. (a) Thermal conductivity measurements at the split cores (PS75/0166 – 235–2) with sampling intervals of 10–25 cm. (b) Overview of sites where gravity corers sampled sediments in the Amundsen Sea Embayment during ANT-XXVI/3 (now PS75) in 2010.

Table 1. Parameterization of Models 1 and 2

Parameterization			Model 1	Model 2
Upper boundary	°C		0	
DBMS	°C		580 [*Langel and Hinze*, 1998]	
Lower boundary	°C		800 [*Hirschmann*, 2000]	
Upper boundary	km		0	
DBMS	km		DBMS (this study)	
Lower boundary	km		25 [*Ritzwoller et al.*, 2001; *Chaput et al.*, 2014]	
Upper crust	Thickness	km	8 [*Kalberg and Gohl*, 2014]	
	Heat capacity c_p	$J\,kg^{-1}\,K^{-1}$	850 [*Eppelbaum et al.*, 2014]	
	Density ρ	$kg\,m^{-3}$	2600 [*Damiani et al.*, 2014; *Kalberg et al.*, 2015]	
	RHP Q_{radio}	$\mu W\,m^{-3}$		
	Conductivity k	$W\,m^{-1}\,K^{-1}$	1 [*Hasterok and Chapman*, 2011] 2.2 [*Kappelmeyer and Haenel*, 1974]	
Lower crust	Thickness	km	17 [*Damiani et al.*, 2014; *Kalberg and Gohl*, 2014]	
	Heat capacity c_p	$J\,kg^{-1}\,K^{-1}$	850 [*Eppelbaum et al.*, 2014]	
	Density ρ	$kg\,m^{-3}$	2800 [*Damiani et al.*, 2014]	
	RHP Q_{radio}	$\mu W\,m^{-3}$		
	Conductivity k	$W\,m^{-1}\,K^{-1}$	0.4 [*Hasterok and Chapman*, 2011] 2.6 [*Kappelmeyer and Haenel*, 1974]	
Intrusions	Thickness	km		0.3–11.3; mean = 4.02 [*Kalberg et al.*, 2015]
	Heat capacity c_p	$J\,kg^{-1}\,K^{-1}$		1050 [*Eppelbaum et al.*, 2014]
	Density ρ	$kg\,m^{-3}$		2900 [*Damiani et al.*, 2014]
	RHP Q_{radio}	$\mu W\,m^{-3}$		2 [*Kipf et al.*, 2012]
	Conductivity k	$W\,m^{-1}\,K^{-1}$		2.6
Model time	Ma		100	100

statistical estimate of Curie point depths and also to map the topography of the magnetic basement. A random and uncorrelated distribution of sources is assumed as a first approximation, although the investigated area might exhibit indeed a variation of magnetic anomaly sources due to a complex crustal architecture. Based on the previous study, the centroid method was introduced which is mostly implemented in the frequency domain, by evaluation the magnetic anomaly of a right-rectangular prism [*Bhattacharyya and Leu*, 1977; *Graf et al.*, 1985]. In this study, the depth to the bottom of the magnetic source (Z_b) is calculated by estimating the depth to the top (Z_t) and centroid depth (Z_0) of the deepest magnetic body. These depths are related to the DBMS (Z_b) as follows:

$$Z_b = 2 \cdot Z_0 - Z_t (km). \tag{1}$$

We applied the centroid method to a gridded magnetic data set that has been collected during two RV Polarstern expeditions ANT-XXIII/4 in 2006 and ANT-XXVI/3 in 2010. The acquisition, processing, and tectonic interpretation of the magnetic anomaly data is published by *Gohl et al.* [2013a]. Their airborne magnetic data were measured with a caesium-vapor magnetometer sensor towed from a helicopter, and complemented by ship-borne magnetic data that were continuously recorded with two three-component fluxgate magnetometer sensors and complemented to airborne magnetic data measured with a caesium-vapor magnetometer sensor. The data processing routine comprised the removal of the International Geomagnetic Reference Field (IGRF), visual editing of obvious erroneous data, and band-pass filtering. Prior to gridding, the differences at cross-points were minimized (leveling) by allowing a plane tolerance of crossing survey line points of 0.0005° (∼50 m). Due to irregular survey line spacing and orientation, a minimum curvature approach during gridding was applied between less sampled areas and those areas with good coverage [*Gohl et al.*, 2013a]. In our study, we used their microleveled [*Ferraccioli et al.*, 1998] grid with 2 km cell size that is shown in Figure 5a overlain by the used helicopter and shipborne magnetic survey tracks.

We evaluated 30 windows of the magnetic anomaly map in the Amundsen Sea, with a dimension of 200 × 200 km and approximately 50% overlapping. The window size was chosen to ascertain that the response of the deepest magnetic layer is captured and disparate tectonic regimes are not averaged. *Ravat et al.* [2007] elaborate that the dimension of the windows analyzed may need to be, in some cases up to 10 times the depth to the bottom, but finds that dimensions of more than 200–300 km are less practical. Together with the uneven data coverage, we find the chosen dimension to suit best our data processing routine and optimize the spatial resolution of the DBMS. The window centers are numbered and marked by black crosses in
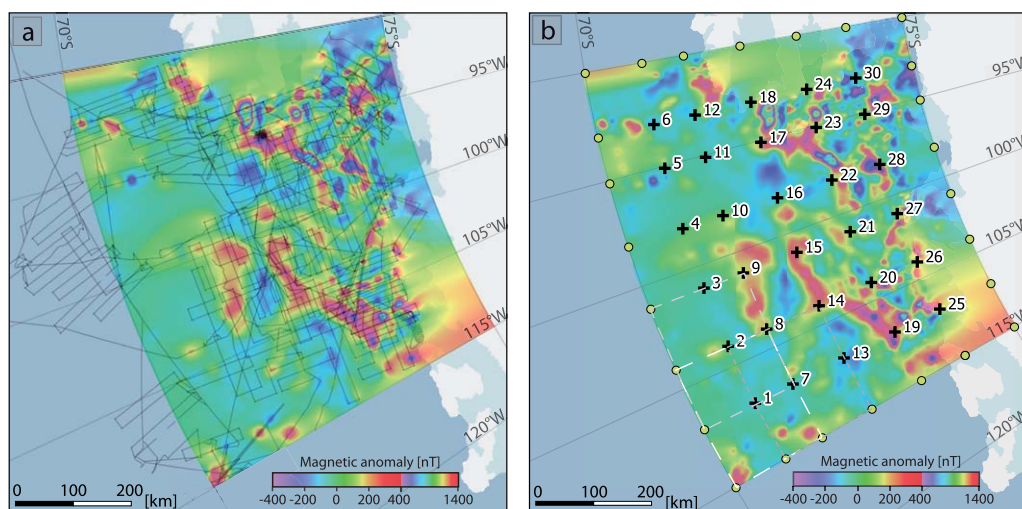
Figure 5. (a) The magnetic anomaly data grid presented by *Gohl et al.* [2013a, 2013b] with 2 km cell size is overlain by helicopter-borne survey lines (fine grey lines) and shipborne survey lines (pink lines) to distinguish areas of less sampled areas and those areas with good coverage. (b) Same grid overlain by centers of the 30 analyzed magnetic anomaly grids, where also the DBMS was projected to. Yellow points indicate extrapolated nearest depth to the bottom of the magnetic source, since the estimated depths represent an average over the entire 200 × 200 km window. Dashed lines indicate three example windows (1, 2, and 7) to demonstrate the geometry and overlapping of the individual windows.

Figure 5b. Within each window we calculated the radially averaged power spectral density using the GMT open source code [*Wessel and Smith*, 1991]. The depths Z_0 and Z_t are obtained in the lower wavenumber (k_r) domain from the slope of the power spectral density (PSD) and the frequency-scaled PSD. We did not high-pass filter the power spectrum before computing the centroid depths. *Bansal et al.* [2011] point out that band-pass filtering in this case is a subjective approach because it is difficult to decide which wavelength should be eliminated. Furthermore, stated by *Ravat et al.* [2007], the longer-wavelength spectrum may contain important information about the magnetic sources. *Tanaka et al.* [1999] suggested computing Z_t from the high wavenumber part of the spectrum, whereas *Bansal et al.* [2011] argue that it may be appropriate for single-layer cases, but for multilayer cases it represents the depth to a shallow layer instead the deepest layer. Visual identification of slope breaks for deriving depths of the sources is considered to be the most subjective part of this method [*Ravat et al.*, 2007]. We treated the slope analysis as conservatively as possible by implementing a MATLAB routine [*The MathWorks Inc.*, 2010] that fits linear regression lines along the slope. Up to a critical wavenumber range ($0.2 <= k_r >= 0.5 \ 2\pi \ km^{-1}$) the regression line is fitted over 4–8 data points in the low wave number regime, resulting in an ensemble of viable depths for Z_t and Z_0, where Z_b can now be obtained from using equation (1). The slope fit and resulting depths are visually demonstrated in Figure 6. The median of this ensemble was used for further calculations in our numerical models. Since the resulting depths are an average for the entire individual window, we also projected the depths to the outer bounds of the outer windows to enhance visualization. These are marked by yellow points in Figure 5b and relate to the nearest estimated depth. *Ravat et al.* [2007] critically examined the real performance of several spectral magnetic depth determination methods in terms of their capability to compute the DBMS based on random and layered magnetic model sources of different thickness. The study finds that the random sources assumption is valid and clear spectral peaks with multiple points are present, then it is possible to determine the DBMS more reliably. We do find the peaks to be clearly visible in 19 out of the 30 windows (e.g., window 6 and 12, Figure 6, top) and in three cases (window 11, 13, and 26) no peak could be distinguished, whereas the remaining eight windows (e.g., 24, Figure 6, top) are debatable. Our error analysis corresponds to the maximum and minimum values of Z_b computed with the slope fitting routine and is demonstrated in Figure 7. The error bars indicate maximum and minimum magnetic source bottom depths of the individual windows.

2.3. Finite Volume Method for 3-D Thermal Models

A program-suite to calculate conductive and advective heat transport in solids was implemented in MATLAB. It was used to create a numerical model which calculates the thermal structure of the working area according to the calculated magnetic basement depths, the measured surface heat flux values and
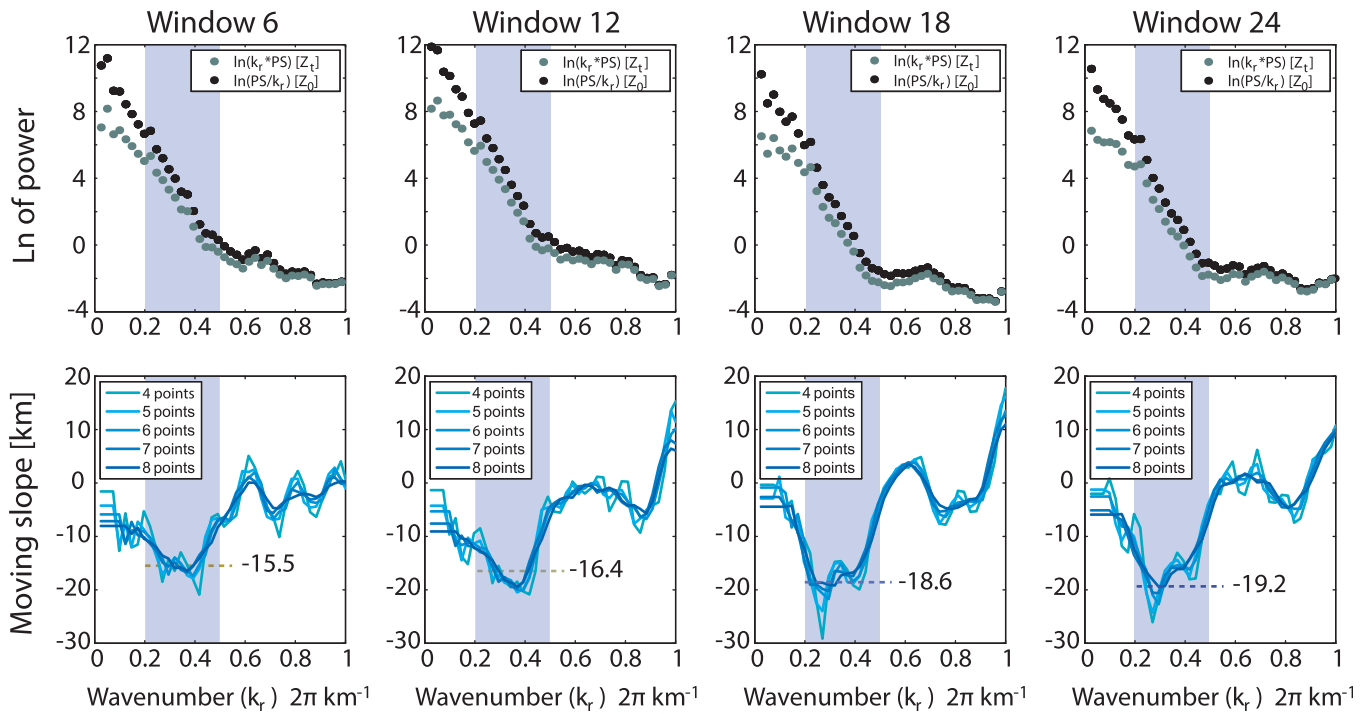
Figure 6. Upper graphs show lower frequency spectrum of the radially averaged power spectral density over wavenumber for window 6, 12, 18, and 24. Corresponding lower graphs show Z_b (DBMS) results of slope analysis. Grey shaded area marks the critical wavenumber range $0.2 <= k_r >= 0.5$ 2π km^{-1}. Here the median depth is calculated over varying point ensembles (4–8) and marked as dashed line in lower graphs and corresponding value. The resulting DBMS for all 30 windows is used as a further constraint in the thermal models of this study.

additional constraint on the crustal architecture by gravimetric and seismic investigations. The suite consists of a list-type input mask, the modular built numerical environment, and a plot-module to visualize temporal and spatial variations of the state and material parameters. The wider-ranging MATLAB code takes radioactive heat production into account and allows for calculation of advective temperature transport, as well as simple phase transitions (isothermal melting or crystallization) on the energetic level. Because the spatial and temporal development of potential rifting processes and/or magmatic intrusions in the offshore region
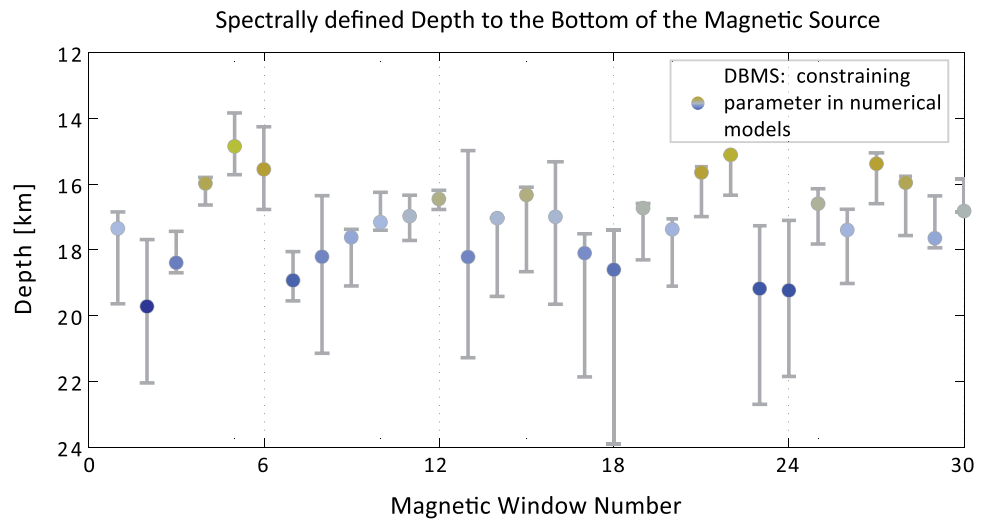
Figure 7. Spectrally derived DBMS (colored circles) for the 30 individual windows with corresponding uncertainties in minimum and maximum values. As demonstrated in Figure 6 the DBMS is calculated from a median depth, which results in an asymmetric distribution within the error ranges.

of the ASE remains speculative, this study neglects advective transport and phase transitions to deliver a simplistic solution of the thermal state by thermal conduction and radioactive heat production. The implementation supports an orthogonal model lattice with predefined thermal material parameters in an initial state. Boundary conditions for the model boundaries and for single cells or cell compounds can be chosen freely. For the chosen boundary conditions, conductive heat transfer and radioactive heat production are calculated until all volume cells reach a thermal equilibrium, hence the temporal derivative of temperature becomes infinitesimal and dT/dt approximates zero.

The implementation applies a finite-difference scheme to solve the Fourier law in a finite volume approach. The Fourier law (equation (2)) gives the heat flow Q in W m^{-2} as the product of the negative derivative of temperature T over space and the thermal conductivity k in W m^{-1} K^{-1}.

$$Q = -\frac{\partial T}{\partial l} * k. \tag{2}$$

Considering a three-dimensional heat transport, combined to the first law of thermodynamics (conservation of energy), gives the heat equation (equation (3)). The temporal derivative of temperature dT/dt calculates as the sum of the spatial derivatives of the heat flow, multiplied by the reciprocals of the material parameters density ρ in kg m^{-1} and specific heat capacity c_p in Jkg^{-1} K^{-1}.

$$\frac{dT}{dt} = \left(\frac{d}{dx}\left(-\frac{dT}{dx}*k_x\right) + \frac{d}{dy}\left(-\frac{dT}{dy}*k_y\right) + \frac{d}{dz}\left(-\frac{dT}{dz}*k_z\right)\right) * \frac{1}{c_p * \rho}. \tag{3}$$

Subsequently, by introducing Q, the equation results in the sum of the directed volumetric heat fluxes in x, y, and z direction and an additional term for internal radioactive heat production Q_{radio} in W m^{-3}, divided by density and specific heat capacity of the volume element (equation (4)).

$$\frac{dT}{dt} = \left(\frac{dQ_x}{dx} + \frac{dQ_y}{dy} + \frac{dQ_z}{dz} + Q_{radio}\right) * \frac{1}{c_p * \rho}. \tag{4}$$

The implicit Euler backward scheme is used to approximate the derivative of temperature over space for the Cartesian x, y, and z coordinates by a differential quotient (equation (5a)). Where l represents the coordinate of a finite volume cell in x, y, or z direction and n is the numerator for the x, y, and z volume element in one of the directions. Using the Euler backward scheme means that the heat flow Q_n is defined as the heat flow from the previous into the actual volume cell (equation (5b)). The thermal conductivity k is calculated as the mean value of the thermal conductivities of the interacting volume elements.

$$\left(\frac{dT}{dl}\right)_n \approx \frac{T_n - T_{n-1}}{l_n - l_{n-1}} = \frac{\Delta T_n}{\Delta l_n}, \tag{5a}$$

$$Q_n \approx -\frac{T_n - T_{n-1}}{l_n - l_{n-1}} * \frac{k_n + k_{n-1}}{2}. \tag{5b}$$

The derivative of heat flux over space, the volumetric heat flow dQ/dl in W m^{-3}, is approximated by the differential quotient of the heat flow over space between the actual and the following volume element (equation (6)), meaning here the explicit Euler forward scheme is used.

$$\left(\frac{dQ}{dl}\right)_n \approx \frac{Q_n - Q_{n+1}}{l_n - l_{n+1}} = \frac{\Delta Q_n}{\Delta l_n}. \tag{6}$$

The equations are applied along with boundary conditions of an isothermal top (ocean/crust interface, 0°C) and an isothermal bottom layer (800°C) while the lateral boundaries are conductively closed, the horizontal temperature gradients are set to zero. The data set of modeled magnetic basement depth (DBMS) is considered by the boundary condition of the Curie temperature occurring at the magnetic basement depth. The model lattice is initialized with the initial material and state parameter for the lattice cells (Table 1). The depth parameterization for the bottom layer was inferred from geophysical investigations [*Damiani et al.*, 2014]. The parametrization of temperature at this depth resulted from modeling the maximum and minimum geotherms (not presented in this study), based on the DBMS estimate ranges. The geotherms indicated reasonable temperatures of 700–900°C at depths of 25 km. Demonstrated in Figure 8 is the grid mesh for model 1 at quasi thermal equilibrium, i.e., changes in temperature with time become infinitesimal (δT/δt
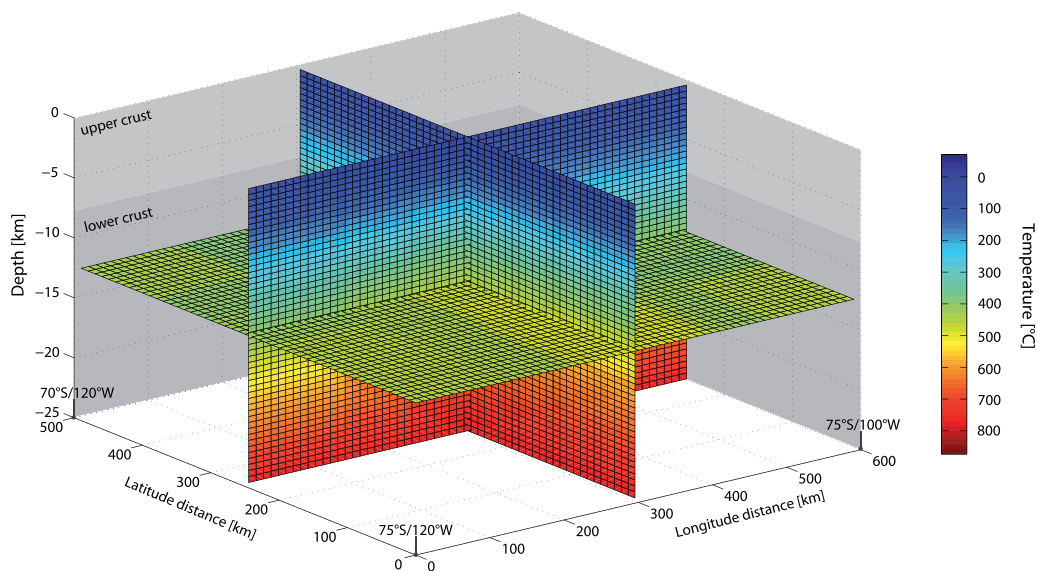
Figure 8. The grid mesh of thermal model 1 is shown at thermal quasi-stationary state, where changes in temperature become infinitesimal small ($\sim 4^{-12}$°C a^{-1}). The height of the individual grid cells is 0.5 km and the width 10 km.

$\approx 4^{-12}$°C a^{-1}). We did not parameterize sedimentary layer [*Gohl et al.*, 2013b], nor constrained the rates of sedimentation, which is a limitation of this model. The blanketing effect of the prerift, synrift, and in particular postrift sediments in a rifted margin setting could in principle have a significant impact on basement heat flux [*Van Wees et al.*, 2009]. The height of the individual grid cells is 0.5 km and the width 10 km.

3. Results and Discussion

3.1. In Situ Geothermal Gradient Measurements

Results of the geothermal heat flux measurements range between 5.5 and 56.5 mW m^{-2}. The in situ measurements were conducted in locations where sedimentary layers are thick enough for the probe to penetrate the seafloor, which are often in small channels or basins. In such locations, warm deep ocean water currents, high sedimentation rates and/or mass wasting events might be expected to bias GHF to lower values. *Jacobs et al.* [2011] illustrate with combined oceanographic measurements in the region from 1994, 2000, and 2007 an increase of temperature and volume of Circumpolar Deep Water (CDW) that intrudes into the continental shelf of the Amundsen Sea at depths >300 m. Their observations suggest that the thermohaline structure in Pine Island Bay exhibits an interannual variability and an increase in CDW temperatures of ~0.1–0.2°C from 1994/2000 compared to 2007/2009. We did not estimate the influence of the warmer bottom water with interannual trends on shallow sediment temperatures to correct the temperature gradients for this effect. Non-existent, long-term observations of the bottom water temperature variations are an essential parameter for this calculation. The spatial variability of the derived heat flux distribution as shown in Figure 2d from the offshore areas in proximity Pine Island Glacier toward the Thwaites Glacier offshore
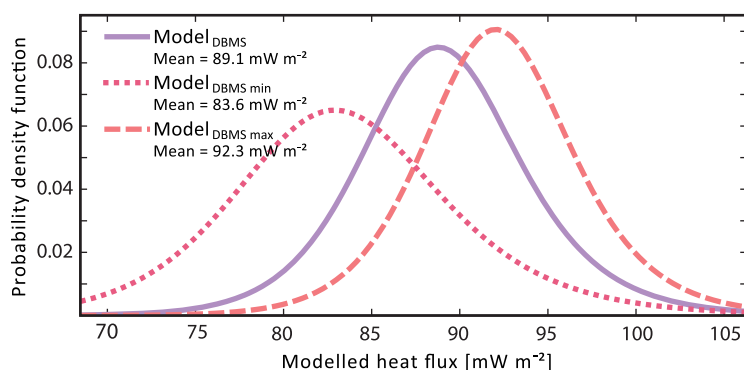
Figure 9. Probability density functions (PDF) that statistically describe the heat flux distribution for three different model runs. The DBMS is a crucial boundary condition, where minimum (Model DBMS min), median (Model DBMS), and maximum (Model DBMS max) values were implemented in the model.
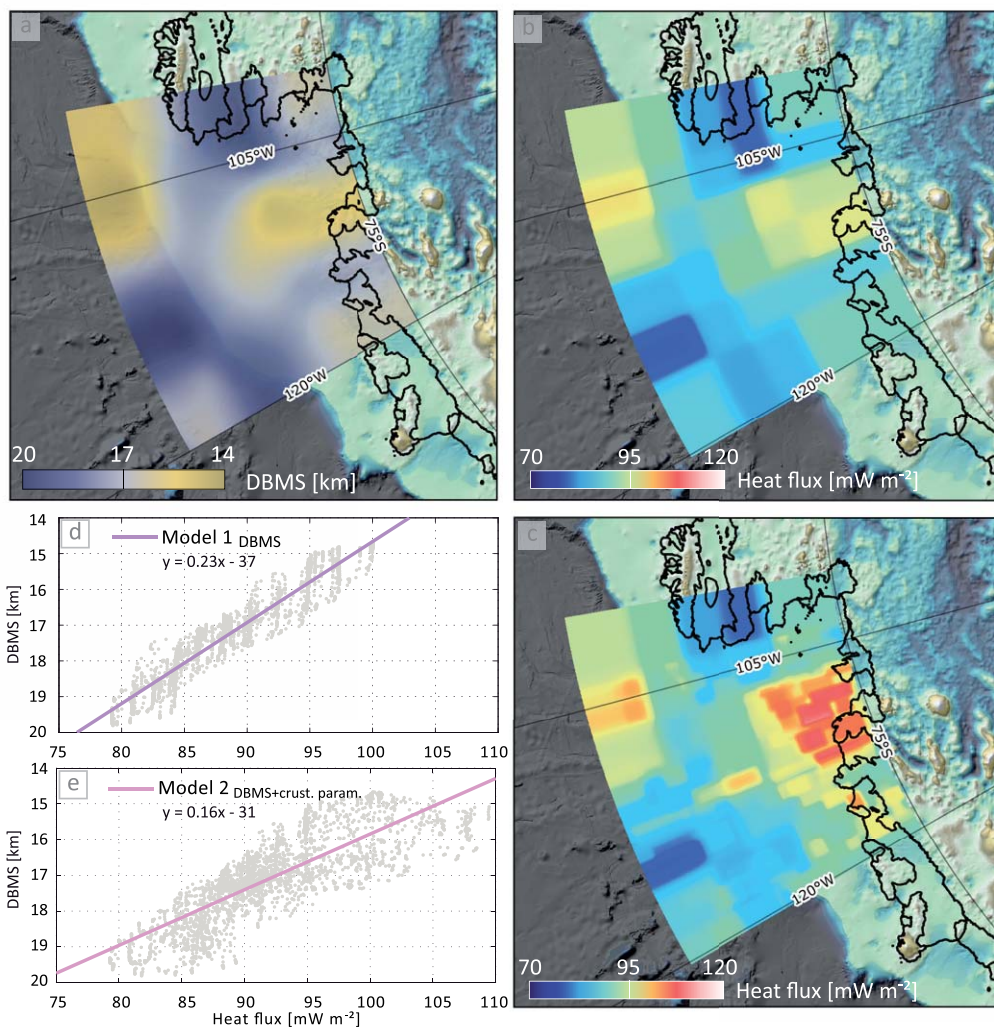
Figure 10. (a) Interpolated map of computed depth to the bottom of the magnetic source values that provide a crucial thermal boundary condition for the 3D FVM models (b, c) presented in this study. Please note that the IBCSO grid in the background of Figures 10a–10c has the same color code as Figure 1. (b) Heat flux computed with model setup 1 and median DBMS values. (c) Heat flux computed with model setup 2 with median DBMS values and additional crustal parameterization. Intrusion bodies presented by *Kalberg et al.* [2015] where considered as an additional source of radiogenic heat production. (d) Results of heat flux estimates for model 1 with respect to the location of the DBMS in the crust. The model data (grey points) are fitted with a linear regression line and show offsets of 1 km. (e) Results of heat flux estimates for model 2, where the model data scatters in a wider range around the linear fit.

area exhibit a clear increase of more than 20 mW m^{-2}. Consequently, we argue that our measurements occur near the lower boundary of the heat flux range in the ASE.

3.2. Depth to the Bottom of the Magnetic Source

DBMS is considered a robust proxy for GHF because of the temperature dependence of magnetization in crustal rocks. DBMS averages for the outer windows were projected to the outer bounds of the model domain in order to obtain a smooth interpolation across the modeled region. DBMS estimates over the model space range between 14.9 and 19.7 km. The absolute values of DBMS can be expected to contain significant error (Figure 7) due to interpretational subjectivity in the method and inhomogeneous data distribution [*Gohl et al.*, 2013a]. Despite this, we can have confidence in the relative values and their trends because they reliably reproduce the spatial variability in magnetization of the crust that can be expected to result from known details of the crustal structure [*Gohl et al.*, 2013a; *Kalberg et al.*, 2015]. For example, a steep gradient that can be followed offshore Thwaites Glacier toward Thurston Island (Figure 10a) potentially reflects a boundary between the Marie Byrd Land block and Thurston Island crustal blocks. Assuming

Table 2. Summary of Geothermal Gradient Stations

Station ID	Longitude (DD.xxxx °W)	Latitude (DD.xxxx °S)	Water Depth (m)	Gradient (°C km^{-1})	Heat Flux (mW m^{-2})
HF 1	−134.1226	−74.5087	893	38.0	38.0
HF 2	−103.4990	−74.8332	1021	18.2	17.1
HF 3	−104.3923	−74.7413	1104	11.7	11.0
HF 4	−105.2005	−74.7473	1302	26.5	24.9
HF 5	−106.6065	−74.6696	1184	31.6	29.7
HF 6	−106.6113	−74.6017	1353	54.9	51.6
HF 7	−106.0000	−74.3333	1386	54.6	51.4
HF 8	−105.5499	−74.2088	1644	44.4	41.8
HF 9	−106.7303	−74.1388	1468	56.8	53.4
HF 10	−105.6923	−74.0015	1037	30.5	28.7
HF 11	−106.7503	−74.0913	604		
HF 12	−106.1847	−74.0417	1111	33.0	31.0
HF 13	−106.2004	−73.5238	806	46.2	43.4
HF 14	−106.1978	−73.5286	813	24.1	22.7
HF 15	−106.2015	−73.5187	814	25.7	24.2
HF 16	−106.2015	−73.5209	795	10.7	10.1
HF 17	−106.2049	−73.5181	795	58.3	45.4
HF 18	−103.3874	−71.8796	752	30.3	28.4
HF 19	−103.3282	−71.7448	768	60.1	56.5
HF 20	−103.0007	−71.4534	626	27.8	26.1
HF 21	−102.3667	−71.0663	1447	32.4	30.4
HF 22	−105.6188	−71.8963	496	59.3	55.8
HF 23	−102.6117	−74.5342	611	5.8	5.5
HF 24	−105.8522	−74.6113	626	15.6	14.6
HF 25	−106.5022	−72.8327	577	34.0	31.9
HF 26	−113.9573	−70.3643	3496	54.4	54.4

that this boundary is expressed by thinner than usual crust, its trend can be traced onshore [*Damiani et al.*, 2014] and correlates to the recently postulated Mt. Murphy Rift (MMR) [*Spiegel et al.*, 2016].

3.3. FVM 3-D Numerical Model 1

In addition to these direct observations of geothermal gradients, a 3-D numerical thermal model focuses on the 300,000 km^2 area between 120°W/75°S and 100°W/70°S. The parametrization of the crust in the model is based on a variety of studies (Table 1) and our estimation of the Depth to the Bottom of the Magnetic Source (DBMS) applying the centroid method [*Ravat et al.*, 2007] on spectral analysis of high-resolution magnetic anomaly data [*Gohl et al.*, 2013a]. To generate a more realistic GHF distribution, we applied the DBMS estimates in a 3-D thermal model of the crust that also incorporates radiogenic heat production [*Kipf et al.*, 2012], density contrasts in upper (0–8 km, 2600 kg m^{-3}) and lower crust (8–25 km, 2800 kg m^{-3}), and thermal conditions at the lithosphere-asthenosphere boundary (800°C, 25 km depth),
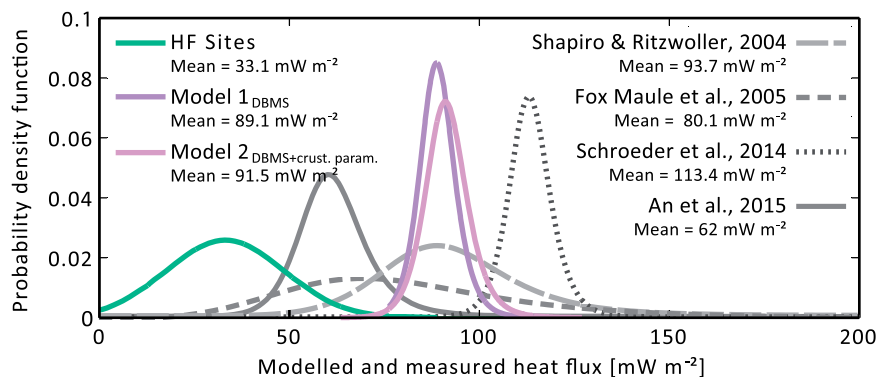
Figure 11. Comparison of best fitting log-logistic probability density function of this study's modeled heat flux, as well as derived from seismic [*Shapiro*, 2004; *An et al.*, 2015], radar [*Schroeder et al.*, 2014], and magnetic [*Fox Maule et al.*, 2005] techniques as applied in Antarctic-wide studies and measured heat flux with a Gaussian distribution. Heat flux values of [*Shapiro*, 2004; *Fox Maule et al.*, 2005; *An et al.*, 2015] extracted from the published continental-scale data sets in the region 80°S/130°W and 70°S/90°W. Entire data set used from [*Schroeder et al.*, 2014], which is concentrated on a regional scale and therefore biased toward higher values. Modeled results correlate best with [*Shapiro*, 2004], which is also shown in the background of Figure 12b.

and surface (0°C, 0 km). The model is built by solving the conductive heat transport equations over a time span of 100 Ma, sufficient for the lithosphere to reach thermal equilibrium by conduction alone (δT/δt $< 4^{-12}$°C a^{-1}). The DBMS is a major boundary condition for the model setup. We computed model 1 with three different DBMS setups and statistically compare the derived heat flux by log-logistic probability density functions (PDF) (Figure 9). Minimum, median, and maximum DBMS depths were implemented and show the range of uncertainties, in which our model estimates the heat flux. The mean values of the statistical distribution range from 89.1 to 92.3 mW m^{-2}, and yield larger offsets toward the lower flanks of the PDF. Offsets in the PDF distribution toward the higher heat flux estimates however decrease strongly toward 105 mW m^{-2}. Shallow DBMS estimates, i.e., maximum values show a vertically stretched shape in the PDF along a smaller range of higher heat fluxes compared to deeper DBMS (minimal) estimate. Heat flux for median DBMS estimates range between of 79 and of 100 mW m^{-2} and the data is presented in map form in Figure 10b.

3.4. FVM 3-D Numerical Model 2 With Further Crustal Parameterization

In a last step, we implemented a yet more realistic crustal model (Figure 10c) taking into account recent interpretations of gravimetric, magnetic anomaly and seismic data for the ASE [*Kalberg et al.*, 2015]. The model features suites of felsic and mafic intrusions, for instance emplaced at the Dorrel Rock intrusive complex during a period of increased magmatic activity at about 30 Ma [*Rocchi et al.*, 2006] to 18 Ma [*Spiegel et al.*, 2016], which disturb the thermal field of the region due to their contrasting thermal conductivity and radiogenic heat production. We do not include the effects of a rising warmer body into our model. The intrusions are represented within the model architecture by the introduction of 25 km wide cells situated
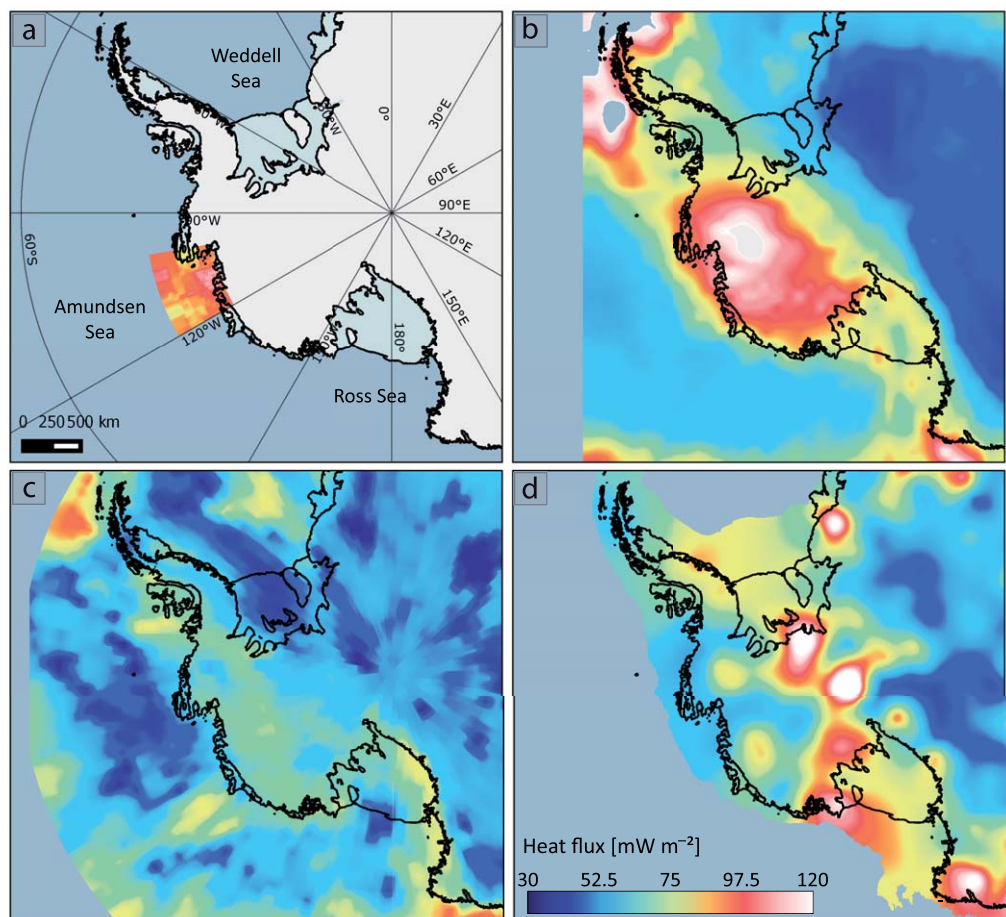
Figure 12. Comparison of different geothermal heat flux data sets in map form. (a) Heat flux estimates computed with model 2 including crustal parameterization. (b) GHF estimates based on seismic tomography present by *Shapiro* [2004] and (c) *An et al.* [2015]. (d) Heat flux estimates published by *Fox Maule et al.* [2005] are derived from satellite magnetic data.

at depths between $\sim$2 and 12 km depth with higher densities (2900 kg m^{-3}, Table 2), elevated heat capacity (1050 J kg^{-1} K^{-1}) and higher radiogenic heat production (2 μW m^{-3}) compared to the ambient crustal rocks. In this most detailed model, GHF ranges between 79 and 109 mW m^{-2}, and the median GHF (91 mW m^{-2}). Although the values resemble those obtained from our previous models, their distribution is most representative of what might be expected based on the known crustal composition. Notably, the additional crustal parameterization leads to higher GHF offshore Thwaites Glacier and toward Marie Byrd Land. Figures 10d and 10e show the results of heat flux estimates for model 1 (Figure 10b) with respect to the location of the DBMS in the crust. The model data (grey points) are fitted with a linear regression line and show offsets of 1 km. The results of heat flux estimates for model 2 (Figure 10c) exhibits a wider range of scattered model data around the linear fit, induced by the additional crustal parameterization in this model.

Log-logistic probability density functions (PDF) are thought to realistically capture the small-scale GHF patterns caused by variations in DBMS [*Shapiro*, 2004], which are controlled by contrasts in crustal thickness and radiogenic heat production. PDF are shown in Figure 11, for both the measured and modeled GHF distributions, by plotting histograms with bin sizes of 2.5 mW m^{-2}. Our modeled GHF distribution overlaps the very broad distribution calculated for West Antarctica based on modeling seismic velocities [*Shapiro*, 2004], but consistently estimates higher GHF than a previous application of spectral techniques to magnetic anomaly data [*Fox Maule et al.*, 2005]. We attribute this to the low-resolution data, measured at satellite altitude, used in the older study. The distribution of our measured GHF values is significantly lower than in all of the models, which we again attribute to the biases implied by the sampling strategy imposed by the sediment temperature probe.

4. Conclusions

The main focus of this paper is the investigation of realistic geothermal heat flux distributions in the Amundsen Sea Embayment, by combining of high-resolution 3-D thermal modeling, depth to the bottom of the magnetic source estimates and in situ temperature measurements. The working area in particular exhibits a challenging region to conduct in situ temperature measurements, because of the thermal variability of bottom water, which is suspected to overprint the thermal signal of the shallow sediment structures. The thermal state over longer time spans is not constrained by long-term bottom water observations, which would permit correcting for this effect. We find a correlation of the measured and modeled heat flux values in terms of spatial variation. Both data sets exhibit highest values offshore Thwaites Glacier along the boundary between Thurston Island and Marie Byrd crustal blocks, but their mean values do differ by a factor of 2.7. *Schroeder et al.* [2014] presented a regional-scale study on geothermal heat flux estimates ($>$100 mW m^{-2}, see Figure 11) in the adjacent onshore region beneath Thwaites Glacier. Their results correlate well with our modeled data in terms of spatial variation and order of magnitude and might be related to a branch of the West Antarctic Rift System and/or Cenozoic intrusions. On a continental-scale perspective our models (e.g., model 2 in Figure 12a) correlate best with geothermal heat flux estimates based on seismic studies (see Figure 12b). Our study finds an average geothermal heat flux of 70–90 mW m^{-2} with strong spatial variations and locally increased values ($>$100 mW m^{-2}) to be most plausible in this sector of the Amundsen Sea Embayment associated to the West Antarctic Rift System. Furthermore, geothermal heat flux measurements in the better understood western Ross Sea Rift sector, which is also part of the West Antarctic Rift System, vary spatially from 76 to 115 mW m^{-2} [*Morin et al.*, 2010]. The methods to determine geothermal heat flux differ in their approach and are limited by data availability, which is a key requirement for future projects in this region. The required validation of onshore and offshore heat flux estimates include, for instance, sea floor drilling projects or applying similar approaches to existing aerogeophysical data sets. These validations will aid the determination of timing and influence of rift-related intrusions on geothermal heat flux patterns and yield likely implications for the adjacent West Antarctic Ice Sheet. Geothermal heat flux is an important control on basal melt pattern and subglacial hydrology, but efforts to quantify its effects on ice sheet dynamics are hampered by the lack of direct observations and also regional-scale geophysical proxies. *Joughin et al.* [2009] for instance discuss increased basin-wide melt rates for Thwaites Glacier compared to Pine Island Glacier assuming a GHF of 70 mW m^{-2}. The sensitivity of basal melting is such that a change in GHF by 10 mW m^{-2} yields a corresponding change in melt rate of 1 mm yr^{-1} [*Joughin et al.*, 2009]. Assuming that the trend of elevated heat flux revealed by our models offshore Thwaites Glacier

continues inland, our results imply a higher influence on basal conditions of the ice sheets in this region, which should be implemented in future thermomechanically coupled ice sheet models.

References

An, M., D. A. Wiens, Y. Zhao, M. Feng, A. Nyblade, M. Kanao, Y. Li, A. Maggi, and J.-J. Lévêque (2015), Temperature, lithosphere-asthenosphere boundary, and heat flux beneath the Antarctic Plate inferred from seismic velocities, *J. Geophys. Res. Solid Earth*, *120*, 8720–8742, doi:10.1002/2015JB011917.

Arndt, J. E., et al. (2013), The international bathymetric chart of the Southern Ocean (IBCSO) version 1.0—A new bathymetric compilation covering circum-Antarctic waters, *Geophys. Res. Lett.*, *40*, 3111–3117, doi:10.1002/grl.50413.

Bansal, A. R., G. Gabriel, V. P. Dimri, and C. M. Krawczyk (2011), Estimation of depth to the bottom of magnetic sources by a modified centroid method for fractal distribution of sources: An application to aeromagnetic data in Germany, *Geophysics*, *76*(3), L11–L22, doi:10.1190/1.3560017.

Bhattacharyya, B. K., and L.-K. Leu (1977), Spectral analysis of gravity and magnetic anomalies due to rectangular prismatic bodies, *Geophysics*, *42*(1), 41–50.

Bingham, R. G., F. Ferraccioli, E. C. King, R. D. Larter, H. D. Pritchard, A. M. Smith, and D. G. Vaughan (2012), Inland thinning of West Antarctic Ice Sheet steered along subglacial rifts, *Nature*, *487*(7408), 468–471, doi:10.1038/nature11292.

Cande, S. C., J. M. Stock, R. D. Müller, and T. Ishihara (2000), Cenozoic motion between east and west Antarctica, *Nature*, *404*(6774), 145–50, doi:10.1038/35004501.

Chaput, J., R. C. Aster, A. Huerta, X. Sun, A. Lloyd, D. Wiens, A. Nyblade, S. Anandakrishnan, J. P. Winberry, and T. Wilson (2014), The crustal thickness of West Antarctica, *J. Geophys. Res. Solid Earth*, *119*, 378–395, doi:10.1002/2013JB010642.

Cochran, J. R. (1983), Effects of finite rifting times on the development of sedimentary basins, *Earth Planet. Sci. Lett.*, *66*, 289–302, doi:10.1016/0012-821X(83)90142-5.

Damiani, T. M., T. A. Jordan, F. Ferraccioli, D. A. Young, and D. D. Blankenship (2014), Variable crustal thickness beneath Thwaites Glacier revealed from airborne gravimetry, possible implications for geothermal heat flux in West Antarctica, *Earth Planet. Sci. Lett.*, *407*, 109–122, doi:10.1016/j.epsl.2014.09.023.

Davey, F. J., R. Granot, S. C. Cande, J. M. Stock, M. Selvans, and F. Ferraccioli (2016), Synchronous oceanic spreading and continental rifting in West Antarctica, *Geophys. Res. Lett.*, *43*, 6162–6169, doi:10.1002/2016GL069087.

Decagon Devices Inc. (2012), *KD2 Pro Thermal Properties Analyzer, Operator's Manual*, 68 pp., Pullman, Wash.

Eagles, G., R. D. Larter, K. Gohl, and A. P. M. Vaughan (2009), West Antarctic Rift System in the Antarctic Peninsula, *Geophys. Res. Lett.*, *36*, L21305, doi:10.1029/2009GL040721.

Eppelbaum, L., I. Kutasov, and A. Pilchin (2014), Thermal properties of rocks and density of fluids, in *Applied Geothermics*, pp. 99–149, Springer, Berlin.

Ferraccioli, F., M. Gambetta, and E. Bozzo (1998), Microlevelling procedures applied to regional aeromagnetic data: An example from the Transantarctic Mountains (Antarctica), *Geophys. Prospect.*, *46*(2), 177–196, doi:10.1046/j.1365-2478.1998.00080.x.

Ferraccioli, F., P. C. Jones, A. P. M. Vaughan, and P. T. Leat (2006), New aerogeophysical view of the Antarctic Peninsula: More pieces, less puzzle, *Geophys. Res. Lett.*, *33*, L05310, doi:10.1029/2005GL024636.

Fisher, A. T., K. D. Mankoff, S. M. Tulaczyk, S. W. Tyler, N. Foley, and the WISSARD Science Team (2015), High geothermal heat flux measured below the West Antarctic Ice Sheet, *Sci. Adv.*, *1*(6), e1500093, doi:10.1126/sciadv.1500093.

Fox Maule, C., M. E. Purucker, N. Olsen, and K. Mosegaard (2005), Heat flux anomalies in Antarctica revealed by satellite magnetic data, *Science*, *309*(5733), 464–467, doi:10.1126/science.1106888.

Fretwell, P., et al. (2013), Bedmap2: Improved ice bed, surface and thickness datasets for Antarctica, *Cryosphere*, *7*(1), 375–393, doi:10.5194/tc-7-375-2013.

Gohl, K. (2012), Basement control on past ice sheet dynamics in the Amundsen Sea Embayment, West Antarctica, *Palaeogeogr. Palaeoclimatol. Palaeoecol.*, *335 336*–, 35–41, doi:10.1016/j.palaeo.2011.02.022.

Gohl, K., and Participants (2010), Reports on polar and marine research: The expedition of the research vessel "Polarstern" to the Amundsen Sea, Antarctica, in 2010 (ANT-XXVI/3), vol. 617, 173 pp., Alfred Wegener Inst. for Polar and Mar. Res., Bremerhaven, Germany.

Gohl, K., A. Denk, G. Eagles, and F. Wobbe (2013a), Deciphering tectonic phases of the Amundsen Sea Embayment shelf, West Antarctica, from a magnetic anomaly grid, *Tectonophysics*, *585*, 113–123, doi:10.1016/j.tecto.2012.06.036.

Gohl, K., G. Uenzelmann-Neben, R. D. Larter, C. D. Hillenbrand, K. Hochmuth, T. Kalberg, E. Weigelt, B. Davy, G. Kuhn, and F. O. Nitsche (2013b), Seismic stratigraphic record of the Amundsen Sea Embayment shelf from pre-glacial to recent times: Evidence for a dynamic West Antarctic ice sheet, *Mar. Geol.*, *344*, 115–131, doi:10.1016/j.margeo.2013.06.011.

Graf, Y., R. J. Okubo, R. O. Hansen, K. Ogawa, and H. Tsu (1985), Curie point depths of the island of Kyushu and surrounding areas, Japan, *Geophysics*, *50*(3), 481–494.

Hansen, J., and R. Greve (1996), Polythermal modelling of steady states of the Antarctic ice sheet in comparison with the real world, *Ann. Glaciol.*, *23*(1), 382–387.

Hasterok, D., and D. S. Chapman (2011), Heat production and geotherms for the continental lithosphere, *Earth Planet. Sci. Lett.*, *307*(1–2), 59–70, doi:10.1016/j.epsl.2011.04.034.

Hirschmann, M. M. (2000), Mantle solidus: Experimental constraints and the effects of peridotite composition, *Geochem. Geophys. Geosyst.*, *1*(10), 1042, doi:10.1029/2000GC000070.

Hughes, T. (2009), Modeling ice sheets from the bottom up, *Quat. Sci. Rev.*, *28*(19–20), 1831–1849, doi:10.1016/j.quascirev.2009.06.004.

Hughes, T. (2011), A simple holistic hypothesis for the self-destruction of ice sheets, *Quat. Sci. Rev.*, *30*(15–16), 1829–1845, doi:10.1016/j.quascirev.2011.04.004.

Jacobs, S. S., A. Jenkins, C. F. Giulivi, and P. Dutrieux (2011), Stronger ocean circulation and increased melting under Pine Island Glacier ice shelf, *Nat. Geosci.*, *4*(8), 519–523, doi:10.1038/ngeo1188.

Jarvis, G. T., and D. P. McKenzie (1980), Sedimentary basin formation with finite extension rates, *Earth Planet. Sci. Lett.*, *48*(1), 42–52, doi:10.1016/0012-821X(80)90168-5.

Jaupart, C., and J.-C. Mareschal (2007), Heat flow and thermal structure of the lithosphere, in *Treatise on Geophysics*, edited by G. Schubert, pp. 217–252, Elsevier, Amsterdam.

Jordan, T. A., F. Ferraccioli, D. G. Vaughan, J. W. Holt, H. Corr, D. D. Blankenship, and T. M. Diehl (2010), Aerogravity evidence for major crustal thinning under the Pine Island Glacier region (West Antarctica), *Geol. Soc. Am. Bull.*, *122*(5–6), 714–726, doi:10.1130/B26417.1.

Jordan, T. A., F. Ferraccioli, and P. T. Leat (2017), New geophysical compilations link crustal block motion to Jurassic extension and strike-slip faulting in the Weddell Sea Rift System of West Antarctica, *Gondwana Res.*, *42*, 29–48, doi:10.1016/j.gr.2016.09.009.

Joughin, I., S. Tulaczyk, J. L. Bamber, D. Blankenship, J. W. Holt, T. Scambos, and D. G. Vaughan (2009), Basal conditions for Pine Island and Thwaites Glaciers, West Antarctica, determined using satellite and airborne data, *J. Glaciol.*, *55*(190), 245–257, doi:10.3189/002214309788608705.

Kalberg, T., and K. Gohl (2014), The crustal structure and tectonic development of the continental margin of the Amundsen Sea Embayment, West Antarctica: Implications from geophysical data, *Geophys. J. Int.*, *198*(1), 327–341, doi:10.1093/gji/ggu118.

Kalberg, T., K. Gohl, G. Eagles, and C. Spiegel (2015), Rift processes and crustal structure of the Amundsen Sea Embayment, West Antarctica, from 3D potential field modelling, *Mar. Geophys. Res.*, *36*(4), 263–279, doi:10.1007/s11001-015-9261-0.

Kappelmeyer, O., and R. Haenel (1974), *Geothermics With Special Reference to Applications*, *Berlin Gebrueder Borntraeger Geoexplor. Monogr. Ser.*, vol. 4, 238 pp., Gebrueder Borntraeger, Berlin.

Kipf, A., N. Mortimer, R. Werner, K. Gohl, P. Bogaard, F. Hauff, and K. A. J. Hoernle (2012), Granitoids and dykes of the Pine Island Bay region, West Antarctica, *Antarct. Sci.*, *12*, 1–12, doi:10.1017/S0954102012000259.

Langel, R. A., and W. J. Hinze (1998), *The Magnetic Field of the Earth's Lithosphere*, Cambridge Univ. Press, Cambridge, U. K.

Larour, E., M. Morlighem, H. Seroussi, J. Schiermeier, and E. Rignot (2012), Ice flow sensitivity to geothermal heat flux of Pine Island Glacier, Antarctica, *J. Geophys. Res.*, *117*, F04023, doi:10.1029/2012JF002371.

LeMasurier, W. E. (2008), Neogene extension and basin deepening in the West Antarctic rift inferred from comparisons with the East African rift and other analogs, *Geology*, *36*(3), 247–250, doi:10.1130/G24363A.1.

Lowe, A., and J. Anderson (2002), Reconstruction of the West Antarctic ice sheet in Pine Island Bay during the Last Glacial Maximum and its subsequent retreat history, *Quat. Sci. Rev.*, *21*(16–17), 1879–1897, doi:10.1016/S0277-3791(02)00006-9.

Luyendyk, B. P., D. S. Wilson, and C. S. Siddoway (2003), Eastern margin of the Ross Sea Rift in western Marie Byrd Land, Antarctica: Crustal structure and tectonic development, *Geochem. Geophys. Geosyst.*, *4*(10), 1090, doi:10.1029/2002GC000462.

McKenzie, D. (1978), Some remarks on the development of sedimentary basins, *Earth Planet. Sci. Lett.*, *40*(1), 25–32, doi:10.1016/0012-821X(78)90071-7.

Morgan, P. (1983), Constraints on rift thermal processes from heat flow and uplift, *Tectonophysics*, *94*(1–4), 277–298, doi:10.1016/0040-1951(83)90021-5.

Morin, R. H., T. Williams, and D. Magens (2010), Heat flow and hydrologic characteristics at the AND-1B borehole, ANDRILL McMurdo Ice Shelf Project, Antarctica, *Geosphere*, *6*(4), 370–378.

Mukasa, S. B., and I. W. D. Dalziel (2000), Marie Byrd Land, West Antarctica: Evolution of Gondwana's Pacific margin constrained by zircon U-Pb geochronology and feldspar common-Pb isotopic compositions, *Bull. Geol. Soc. Am.*, *112*(4), 611–627, doi:10.1130/0016-7606(2000)112 < 611:MBLWAE>2.0.CO;2.

Payne, A. J., A. Vieli, A. P. Shepherd, D. J. Wingham, and E. Rignot (2004), Recent dramatic thinning of largest West Antarctic ice stream triggered by oceans, *Geophys. Res. Lett.*, *31*, L23401, doi:10.1029/2004GL021284.

Pfender, M., and H. Villinger (2002), Miniaturized data loggers for deep sea sediment temperature gradient measurements, *Mar. Geol.*, *186*, 557–570.

Pollard, D., R. M. DeConto, and A. A. Nyblade (2005), Sensitivity of Cenozoic Antarctic ice sheet variations to geothermal heat flux, *Global Planet. Change*, *49*(1–2), 63–74, doi:10.1016/j.gloplacha.2005.05.003.

Ravat, D., A. Pignatelli, I. Nicolosi, and M. Chiappini (2007), A study of spectral methods of estimating the depth to the bottom of magnetic sources from near-surface magnetic anomaly data, *Geophys. J. Int.*, *169*(2), 421–434, doi:10.1111/j.1365-246X.2007.03305.x.

Ritzwoller, M. H., N. M. Shapiro, A. L. Levshin, and G. M. Leahy (2001), Crustal and upper mantle structure beneath Antarctica and surrounding oceans, *J. Geophys. Res.*, *106*(12), 30,645–30,670, doi:10.1029/2001JB000179.

Rocchi, S., W. E. LeMasurier, and G. Di Vincenzo (2006), Oligocene to Holocene erosion and glacial history in Marie Byrd Land, West Antarctica, inferred from exhumation of the Dorrel Rock intrusive complex and from volcano morphologies, *Bull. Geol. Soc. Am.*, *118*(7–8), 991–1005, doi:10.1130/B25675.1.

Schroeder, D. M., D. D. Blankenship, D. A. Young, and E. Quartini (2014), Evidence for elevated and spatially variable geothermal flux beneath the West Antarctic Ice Sheet, *Proc. Natl. Acad. Sci. U. S. A.*, *111*(25), 9070–9072, doi:10.1073/pnas.1405184111.

Shapiro, N. (2004), Inferring surface heat flux distributions guided by a global seismic model: Particular application to Antarctica, *Earth Planet. Sci. Lett.*, *223*(1–2), 213–224, doi:10.1016/j.epsl.2004.04.011.

Spector, A., and F. Grant (1970), Statistical models for interpreting aeromagnetic data, *Geophysics*, *35*(2), 293–302.

Spiegel, C., J. Lindow, P. J. J. Kamp, O. Meisel, S. Mukasa, F. Lisker, G. Kuhn, and K. Gohl (2016), Tectonomorphic evolution of Marie Byrd Land—Implications for Cenozoic rifting activity and onset of West Antarctic glaciation, *Global Planet. Change*, *145*, 98–115, doi:10.1016/j.gloplacha.2016.08.013.

Tanaka, A., Y. Okubo, and O. Matsubayashi (1999), Curie point depth based on spectrum analysis of the magnetic anomaly data in East and Southeast Asia, *Tectonophysics*, *306*(3–4), 461–470, doi:10.1016/S0040-1951(99)00072-4.

The MathWorks Inc. (2010), MATLAB version 7.10.0, Natick, Mass.

Van Wees, J. D., F. van Bergen, P. David, M. Nepveu, F. Beekman, S. Cloetingh, and D. Bonté (2009), Probabilistic tectonic heat flow modeling for basin maturation: Assessment method and applications, *Mar. Pet. Geol.*, *26*(4), 536–551, doi:10.1016/j.marpetgeo.2009.01.020.

Wessel, P., and W. H. F. Smith (1991), Free software helps map and display data, *Eos Trans. AGU*, *72*(41), 2324–9250.

Wingham, D. J., D. W. Wallis, and A. Shepherd (2009), Spatial and temporal evolution of Pine Island Glacier thinning, 1995–2006, *Geophys. Res. Lett.*, *36*, L17501, doi:10.1029/2009GL039126.